Photothermal camera port accessory for microscopic thermal diffusivity imaging

Facundo Zaldívar Escola
Darío Kunik
Nelly Mingolo
Oscar Eduardo Martínez

SPIE.

Photothermal camera port accessory for microscopic thermal diffusivity imaging

Facundo Zaldívar Escola,[a] Darío Kunik,[b] Nelly Mingolo,[a,*] and Oscar Eduardo Martínez[a]
[a]Universidad de Buenos Aires, Facultad de Ingeniería, Paseo Colón 850, Buenos Aires 1063, Argentina
[b]Tolket S.R.L., Av. Gral. Las Heras 3923, Of. 6E, Buenos Aires 1425, Argentina

Abstract. The design of a scanning photothermal accessory is presented, which can be attached to the camera port of commercial microscopes to measure thermal diffusivity maps with micrometer resolution. The device is based on the thermal expansion recovery technique, which measures the defocusing of a probe beam due to the curvature induced by the local heat delivered by a focused pump beam. The beam delivery and collecting optics are built using optical fiber technology, resulting in a robust optical system that provides collinear pump and probe beams without any alignment adjustment necessary. The quasiconfocal configuration for the signal collection using the same optical fiber sets very restrictive conditions on the positioning and alignment of the optical components of the scanning unit, and a detailed discussion of the design equations is presented. The alignment procedure is carefully described, resulting in a system so robust and stable that no further alignment is necessary for the day-to-day use, becoming a tool that can be used for routine quality control, operated by a trained technician. © 2016 Society of Photo-Optical Instrumentation Engineers (SPIE) [DOI: 10.1117/1.OE.55.6.064110]

1 Introduction

The determination of thermophysical properties at microscopic levels supplies crucial information for the characterization and development of materials and devices, also giving information on materials homogeneity, phase structure, and transport properties. Photothermal techniques provide a unique opportunity to explore thermal properties at microscopic scales and have been used for the characterization of layered materials,[1,2] to obtain nondestructive depth profiles,[3–5] for the characterization of microstructure homogeneity of sintered nuclear fuels,[6,7] mapping composition–phase–property relationships across phase boundaries,[8–10] to provide noncontact information on surface hardening of steels,[11–13] and nanoparticle imaging and characterization,[14–18] among many other applications.

All techniques share a common heat source and a modulated or pulsed laser beam directed to the region to be analyzed. The different probe mechanisms make the distinction between the large diversity of techniques available. Detecting the infrared radiation from the heated surface (IR radiometry) has proven a very reliable and practical technology for opaque materials (particularly metals) explored at mesoscopic scales and for depth profiling.[3–5,12] The difficulty in exploring this technique at microscopic levels resides mainly in the dependence of the IR emission on the size of the heated area and the high thermal noise of the IR detectors. The best resolution at microscopic levels has been achieved with nanoparticle detection by thermal lensing in transparent surrounding media,[14,15] which has proven a very powerful technique for biological research.[16–18] For absorbing materials such as metals and strongly scattering media such as sintered ceramics, microscopic exploration

has been done, probing the change in reflection with the temperature (thermoreflectance) performed either measuring the phase lag in the modulation of the probe beam in the frequency domain[19–21] or with a pump and probe technique in the time domain with very short laser pulses.[22,23] Results have also been reported deflecting a grazing probe beam (mirage effect),[24] or deflecting a beam in the curved surface induced by a localized thermal expansion.[6,25–28]

All the mentioned microscopic techniques described previously have been developed as custom-build instruments and have very strict restrictions regarding the beam pointing stability and require very careful and frequent realignment. A photothermal technique that makes use of optical fiber technology developed for optical communications has yielded a very robust system,[29] that provides by construction collinear pump and probe beams. A confocal detection mechanism was used to measure the thermal properties by sensing the defocusing of the probe beam at the pump modulation frequency. The defocusing was due to the surface curvature induced by the local thermal expansion of the material generated by the pump beam. It is important to stress that reinjecting in the optical fiber has more stringent restrictions than collecting with a pinhole as used in standard confocal systems. For pinholes, smaller returning beam yield larger throughputs and the angular acceptance is large, having no restrictions in the phase front curvature at the pinhole. Optical fibers have very restrictive requirements in the amplitude and phase profiles, as the field mode must match the fiber mode for optimal coupling. This was discussed in detail before[30] showing the different relevant parameters and the system sensitivity to misplacement or misalignment of the optical elements or the sample.

---

*Address all correspondence to: Nelly Mingolo, E-mail: nmingol@fi.uba.ar

The remaining challenge was to include such a robust design as an accessory of commercial microscopes.[31] This required a shift in the operating wavelength from the near-infrared used for optical communications[29,30] to wavelength in the visible range where the microscopes are typically optimized. Such accessory was applied to the characterization of sintered mixed oxides.[31] It was shown how to retrieve thermal diffusivity from phase delay in the modulation of the probe beam. No detailed description of the equipment design was given. In this work, we will present the design equations for the system as well as the detail of requirements and constraints for the fabrication of this instrument.

A galvanometric scanning unit, typically used in confocal and other scanning microscopes, was also added. This is not a plug-and-play technology for the reasons discussed before regarding the reinjection requirements for a fiber, and very specific conditions must be met for an adequate reinjection profile covering the entire field of view of the microscope camera. This is part of the discussion carried out in Sec. 4. After taking care of the adequate conditions, the instrument results are very robust, allowing a day-to-day use, without the need for realignment. Detailed aligning procedure is described and results are presented for several samples to illustrate the capability of the system.

2 Description of the Technique

The technique relies on heating a surface with a focused modulated pump beam and analyzing the induced surface curvature at microscopic levels due to the modulated thermal expansion and recovery using a second probe beam collinear with the pump beam. Even though the pump laser is absorbed at the sample surface, the heat flows into the bulk of the sample a distance of the order of the beam diameter. The surface deformation results from the thermal expansion of the heated volume. As the incidence of the beams is by design perpendicular to the sample, the reflected power is in general insensitive to light polarization. Typical experimental situations include a thin Pt film (20 nm) that determines the optical properties of the sample and present no

anisotropy. Hence, the polarization anisotropy will be neglected in the following description.

The two beams are delivered by the same single-mode optical fiber as shown in Fig. 1(b), thus guaranteeing the colinearity. The reflected probe beam is collected by the same fiber (that is not exactly at the focus), and the amount of reinjected power is then dependent on the defocusing introduced by the curvature induced in the sample surface. A schematic of this description is shown in Fig. 1(a).

The signal results from the measurement of the reinjected probe beam power at the pump beam modulation frequency (ω) of the pump beam that were shown to be[29]

$$S = \beta h(\omega/\omega_o), \tag{1}$$

where

$$\beta = \frac{(1 - R')}{4\kappa_r} \frac{P_\omega P_P \lambda_z R}{\lambda_{\text{probe}}} \frac{d\tau}{dQ}\bigg|_{Q=0} \left(\frac{w}{\sigma}\right)^2 \tag{2}$$

and h is a complex function that depends only on the frequency normalized by the critical frequency ω_0, defined as

$$\omega_0 = 2D/\sigma^2, \tag{3}$$

where D is the thermal diffusivity of the sample at the impinging location and σ is the pump laser Gaussian beam radius. R' is the reflectivity of the sample at the pump wavelength, P_ω is the pump power modulation amplitude, P_P is the probe power, λ_z is the sample thermal expansion coefficient, R is the sample reflectivity at the probe wavelength, κ_r is the sample transverse thermal conductivity, λ_{probe} is the probe wavelength, Q is the surface curvature (inverse of the radius of curvature), τ is the throughput of the system (fraction of the probe power reinjected into the fiber), and w is the Gaussian probe beam diameter at the sample surface.

As $h(\omega/\omega_0)$ is known and changes more rapidly when the modulation frequency is of the order of the critical frequency,[29] measuring the signal phase at a known frequency
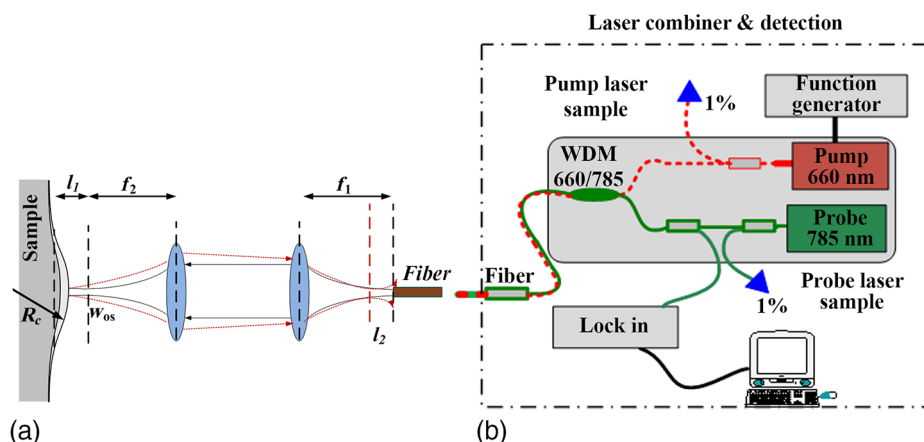

Fig. 1 (a) Scheme of the optical setup. The pump and probe beam emerge from the optical fiber and are focused to the sample surface by the two lenses of focal distance f_1 and f_2. The sample and the fiber are out of plane at distance l_1 and l_2. The pump beam heats the surface that expands developing a curved profile of radius R_c. The probe beam is back reflected and partially collected by the same fiber. w_{os} is the Gaussian beam waist on the sample side. (b) Laser combiner and detection unit, wavelength division multiplexer (WDM; combiner). Pump and probe lasers are attached to the optical setup by means of a connectorized optical fiber.

provides the information on the thermal diffusivity without any additional knowledge of the parameters appearing in β, which only affects the amplitude of the signal.[31]

3 Experimental Setup

In Fig. 2, a modular scheme and a photograph of the setup is presented. The main modules can be distinguished. One is the microscope, a commercial device that in our case is an Olympus BX51 upright unit. The second one is the scanning accessory (SA), similar to the units typically used in other scanning microscopy techniques but with particular design constraints due to the need to reinject the reflected light into the optical fiber used for beam delivery and collection. The third stage, shown in Fig. 1(b), integrated by the pump and probe lasers; the optical fiber network that combines the beams and redirects the collected power from the reflection toward the detection system and the detection system itself appears physically separated and connected by a fiber patch cable.

The main difference with the simple scheme shown in Fig. 1 is that a scanner is included and the optical system consists of two telescopes in tandem: one is the microscope and the other one is the scanning optics. The scanner is coupled into the microscope through a second camera port in such a way that the scanning unit generates a focused scanned beam on the camera (image) plane of the microscope. The perfectly focused configuration would be when $\Delta, \delta_1, \delta_2, \delta_3, \delta_4, \delta_5$ are all zero, which is if the successive back and front focal planes of the lenses all coincide and the tilt plane of the scanner is located exactly at the coinciding focal planes of the lenses L_{C1} and L_1. If these conditions could be met all the analyses made would be valid and no additional design and alignment considerations would be needed. Nevertheless these conditions cannot be fulfilled because in commercial microscopes no special care is taken to provide a value $\Delta = 0$ and the position of the

scanning mirrors in the x- and y-directions are located a certain distance (10 mm in our case) yielding a minimum value for δ_1 and δ_3. It is mandatory then to determine the limitations these restrictions impose in a real system. Qualitatively, the problem is that for different scan angles (sample location) the reflected probe beam changes the angle of incidence at the fiber tip, reducing the reinjected power. The focal distances are: $f_{LC1} = 4.6$ mm, $f_{L1} = 175$ mm, $f_{L2} = 180$ mm, and $f_{ob} = 18$ mm (for a $10\times$ magnification). The offset of the tube lens in this microscope is $\Delta = 21 \pm 1$ mm.

4 Design Equations

The parameter δ_5 can be adjusted in the alignment procedure as discussed later and hence will be set to zero for our calculations. The parameter δ_4 is the same parameter that appears in the two lens schemes presented as l_1 in Fig. 1(a) and will also be discussed separately. The parameter Δ usually is not null and depends on the particular microscope and is set by the manufacturer. The parameter δ_1 cannot be set to zero for both scanning mirrors unless additional optics and complexity is added to image the center of one scanning mirror into the center of the other one.[32] We will include this parameter and use δ_3 as a corrective degree of freedom. The experimental acceptable range for δ_3 is relevant information as it represents the region where additional optics can be added, such as an automatic focus correction device.

For the propagation of the Gaussian laser beams across the optical system, the well-known $ABCD$ matrices[33] were used extended to a 3×3 dimension to account for the tilt introduced by the scanning mirrors[30] and to study the sensitivity to misalignment. The matrices have six significant elements and provide the output transverse coordinate x' and the propagating angle θ' as a function of the input parameters x and θ
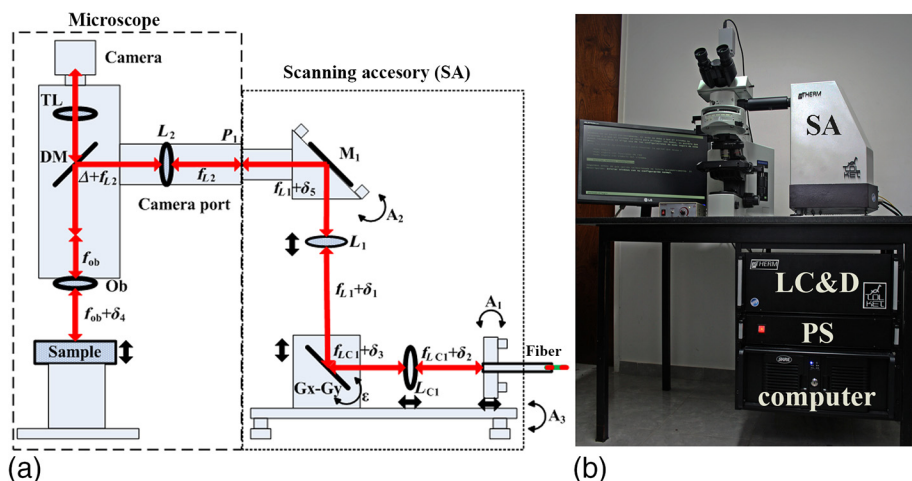

Fig. 2 Experimental setup. (a) Optics schematic. Module I: commercial microscope with two camera ports. Module II: SA. The parts: L_{C1}, collimating lens (coupled to the fiber with adjustable focus); Gx_Gy, two-axis galvoscanner; L_1, scanning lens; M_1, mirror; L_2 and TL, tube lenses; DM, dichroic mirror; Ob, objective lens; A_1, kinematic mount for fiber tip; A_2, kinematic 90 deg steering mount for mirror M_1; A_3, tilt platform; WDM, wavelength division multiplexer (combiner). P_1, camera plane; $f_{LC1}, f_{L1}, f_{L2}, f_{ob}$ are focal distances for lenses L_{C1}, L_1, L_2, and objective. $\delta_1, \delta_2, \delta_3, \delta_4$, and Δ are the offset distances from coincident focal planes of successive lenses. ε is the angular displacement made to scan the sample. (b) Photograph of the complete system. SA, scanning accessory; LC&D, laser combiner and detection unit; PS, power supply. The computer includes the lock-in amplifier.

$$\begin{bmatrix} x' \\ \theta' \\ 1 \end{bmatrix} = \begin{bmatrix} A & B & E \\ C & D & F \\ 0 & 0 & 1 \end{bmatrix} \begin{bmatrix} x \\ \theta \\ 1 \end{bmatrix}, \tag{4}$$

where A, B, C, and D are the well-known terms for Gaussian beam propagation, E accounts for an error in the centering of the optical component respect to the system axis (it is simply the lateral shift of the axis respect to the center of the incoming beam), and F accounts for the misalignment of the element (it is equal to the tilt angle between the axis of consecutive optical elements). As Eq. (4) is applied for consecutive optical elements and free-space propagations, the overall matrix for a system is simply the product of the successive matrices of the components placing the matrix for the first element to the right and the last one to the left. The Gaussian beam parameters at the output of the system are obtained in the usual manner with the $ABCD$ submatrix. The center of the Gaussian beam is given by the E coefficient (provided that we started with a centered beam). Similarly, the tilt angle of the Gaussian beam is given by the F parameter.

As for the well-centered elements, it is $E = F = 0$, the propagation from the scanning mirror to the sample and back can be analyzed using the $ABCD$ submatrix and extending it afterward to 3×3.

The matrices M_d for propagating a distance S and M_L for a thin lens of focal distance f are

$$M_d(s) = \begin{pmatrix} 1 & S \\ 0 & 1 \end{pmatrix}, \tag{5}$$

$$M_L(f) = \begin{pmatrix} 1 & 0 \\ -1/f & 1 \end{pmatrix}. \tag{6}$$

Hence, the forward trip from the scanning mirror to the sample will be represented by the matrix

$$M = M_d(f_{ob})M_L(f_{ob})M_d(L)M_L(f_{L2})M_d(f_{L2} \\ + f_{L1})M_L(f_{L1})M_d(f_{L1} + \delta_1), \tag{7}$$

where $L = f_{ob} + \Delta + f_{L2}$. After multiplying the matrices

$$M = \begin{bmatrix} 0 & -f_{ob}\frac{f_{L1}}{f_{L2}} \\ \frac{f_{L2}}{f_{ob}f_{L1}} & \frac{1}{f_{ob}}\left(\Delta\frac{f_{L1}}{f_{L2}} + \delta_1\frac{f_{L2}}{f_{L1}}\right) \end{bmatrix} = \begin{pmatrix} a & b \\ c & d \end{pmatrix}. \tag{8}$$

The requirement for the system is that a ray entering at an angle ε through the center of the optical system hits the sample (exits the system) in normal direction at a lateral coordinate x, giving in this manner, a scanning beam that is reflected over its path. Hence, we request

$$M\begin{pmatrix} 0 \\ \varepsilon \end{pmatrix} = \begin{pmatrix} a & b \\ c & d \end{pmatrix}\begin{pmatrix} 0 \\ \varepsilon \end{pmatrix} = \begin{pmatrix} x \\ 0 \end{pmatrix} \Rightarrow d = 0, \tag{9}$$

which yields from Eq. (8)

$$d = \frac{1}{f_{ob}}\left(\Delta\frac{f_{L1}}{f_{L2}} + \delta_1\frac{f_{L2}}{f_{L1}}\right) = 0 \Rightarrow \delta_{1i} = -\Delta\frac{f_{L1}^2}{f_{L2}^2} \\ = -20.3 \text{ mm}, \tag{10}$$

where δ_{1i} is the ideal value for δ_1 (that cancels d). But as the pivot point from the two scanning mirrors does not coincide, the best option is to locate the two mirrors symmetrically with

$$\delta_1 = \delta_{1i} \pm L_e, \tag{11}$$

where L_e is half the distance between scanning mirrors (that for our setup is $L_e = 5$ mm). For this case

$$d = \frac{1}{f_{ob}}\left(\pm L_e\frac{f_{L2}}{f_{L1}}\right). \tag{12}$$

To compute the reinjected power the return matrix M_R from the sample to the scanning mirror must be computed, and it is obtained by multiplying all the matrices used to obtain M in reverse order, yielding

$$M_R = \begin{pmatrix} d & b \\ c & 0 \end{pmatrix}. \tag{13}$$

In a similar way, the matrix describing the optical system from the fiber tip to the scanning mirrors M_F is computed

$$M_F = M_d(f_{LC1} + \delta_3)M_L(f_{LC1})M_d(f_{LC1} + \delta_2) \\ = \begin{pmatrix} -\frac{\delta_3}{f_{L2}} & f_{L2} - \frac{\delta_2\delta_3}{f_{L2}} \\ -\frac{1}{f_{L2}} & -\frac{\delta_2}{f_{L2}} \end{pmatrix} \tag{14}$$

and the returning matrix M_{FR} from the scanning mirrors to the fiber is obtained by exchanging δ_3 with δ_2. Finally to obtain the full round trip information from the fiber tip, the tilting from the scanning mirrors must be intercalated between M_F and M and between M_R and M_{FR}. For this purpose, the matrices must be extended to 3×3 dimensions. For M_F

$$M_F = \begin{pmatrix} -\frac{\delta_3}{f_{L2}} & f_{L2} - \frac{\delta_2\delta_3}{f_{L2}} & 0 \\ -\frac{1}{f_{L2}} & -\frac{\delta_2}{f_{L2}} & 0 \\ 0 & 0 & 1 \end{pmatrix} \tag{15}$$

and similarly for the other matrices. For the tilt from the scanner

$$M_\varepsilon = \begin{pmatrix} 1 & 0 & 0 \\ 0 & 1 & \varepsilon \\ 0 & 0 & 1 \end{pmatrix} \tag{16}$$

and the full round trip matrix M_T results

$$M_T = M_{FR} M_\varepsilon M_R M M_\varepsilon M_F = \begin{pmatrix} A & B & E \\ C & D & F \\ 0 & 0 & 1 \end{pmatrix}$$

$$= \begin{pmatrix} 1 - 2\frac{\delta_2 \delta_3}{f_{L2}^2} - L_e \frac{\delta_2}{f_{L2}^2} & 2\delta_2 \left(1 - 2\frac{\delta_2 \delta_3}{f_{L2}^2}\right) - L_e \frac{\delta_2^2}{f_{L2}^2} & \varepsilon L_e \frac{\delta_2}{f_{L2}} \\[2mm] -\frac{L_e}{f_{L2}^2} - \frac{2\delta_3}{f_{L2}^2} & 1 - 2\frac{\delta_2 \delta_3}{f_{L2}^2} - L_e \frac{\delta_2}{f_{L2}^2} & \varepsilon\frac{L_e}{f_{L2}} \\[2mm] 0 & 0 & 1 \end{pmatrix}.$$

(17)

Notice that the sample was assumed a flat mirror (with no thermal deformations). The defocusing due to the deformation has a very small contribution to the reinjected power[29,30] that does not contribute significantly to the total round trip reinjected power computed in this section. It is only significant in the modulated component.

With this round trip matrix, the reinjected power can be computed[30] assuming a Gaussian field distribution exiting the fiber tip

$$\psi_1 = A_1 e^{\frac{-ik(x^2+y^2)}{2q_1}}$$

(18)

and the return field

$$\psi_2 = A_2 e^{\frac{-ik[(x-x_0)^2+y^2]}{2q_2}} e^{-ik\alpha x},$$

(19)

where A_1 and A_2 are normalizing constants to keep constant power (losses neglected), q_1 and q_2 are the well-known Gaussian beam parameter (related to the beam size and phase front curvature), x_0 is the lateral displacement of the beam, and α is the tilt. The q parameters are related through the round trip matrix as

$$q_2 = \frac{Aq_1 + B}{Cq_1 + D}$$

(20)

and the tilt and displacement are

$$\begin{pmatrix} x_0 \\ \alpha \\ 1 \end{pmatrix} = M_T \begin{pmatrix} 0 \\ 0 \\ 1 \end{pmatrix} = \begin{pmatrix} E \\ F \\ 1 \end{pmatrix}.$$

(21)

From the overlap integral between ψ_1 and ψ_2,[34] the reinjected fraction T can be computed[30] yielding

$$T = |\gamma|^2 = \frac{4}{\left(\frac{w_2}{w_1} + \frac{w_1}{w_2}\right)^2 + \left(\frac{kw_1 w_2}{2R_2}\right)^2} e^{-(\zeta + \zeta^*)},$$

(22)

where

$$\zeta = \frac{\left(\frac{1}{w_2^2} + \frac{ik}{R_2}\right) x_0^2 \left(\frac{1}{w_1^2} + \frac{ik\alpha}{x_0}\right) + \left(\frac{\alpha k}{2}\right)^2}{\left(\frac{1}{w_2^2} + \frac{1}{w_1^2} + \frac{ik}{2R_2}\right)},$$

(23)

where w_1 and w_2 are the beam sizes and R_2 is the phase front curvature, obtained from the q parameter as

$$\frac{1}{q_n} = \frac{1}{R_n} - \frac{2i}{kw_n^2} \quad n = 1,2.$$

(24)

and $1/R_1 = 0$.

5 Tolerance to Misplacement

With the equations derived, the value of the reinjected fraction T can be computed for different values of the parameters δ_2 and δ_3. For δ_2, it was observed that the only effect is to defocus the returning beam, reducing the coupling, but as it does not produce a significant tilt in the beam, the incidence on the sample is almost normal along the entire scan, not introducing a reduction in the field of view (scanning range).

The transmission as a function of δ_3 and the scanning distance is presented in Fig. 3 for $\delta_1 = \delta_{1i} + L_e$ and for a fixed value of $\delta_2 = z_0/2$ (z_0 is the confocal parameter at the output of the fiber and $z_0 = 35~\mu m$ for our case). The acceptable range for δ_3 is large enough to fit an additional device in the beam path if needed. Within this range and with the scanning range displayed, the relative loss in transmission for the system is only 10% of the maximum, indicating that for the present design conditions, the parameter δ_3 can be varied without much precaution within the indicated values. Much larger distances would give rise to significant loss in the signal. Regarding the losses introduced by the scanning, they add only a 2% within the range plotted that equals the field of view of our camera. This scanning loss is due to the impossibility of setting $\delta_1 = \delta_{1i}$.

The last shifting parameter to be considered is δ_4, which must be set away from perfect focus in order for the signal to appear.[29] Including this parameter, changes the matrices M and M_R, being now

$$M = \begin{pmatrix} a & b \\ c & d \end{pmatrix} = \begin{pmatrix} \delta_4 \frac{f_{L2}}{f_{ob} f_{L1}} & -f_{ob} \frac{f_{L1}}{f_{L2}} + \delta_4 \frac{L_e}{2} \frac{f_{L2}}{f_{ob} f_{L1}} \\[2mm] \frac{f_{L2}}{f_{ob} f_{L1}} & \frac{L_e}{2} \frac{f_{L2}}{f_{ob} f_{L1}} \end{pmatrix},$$

(25)

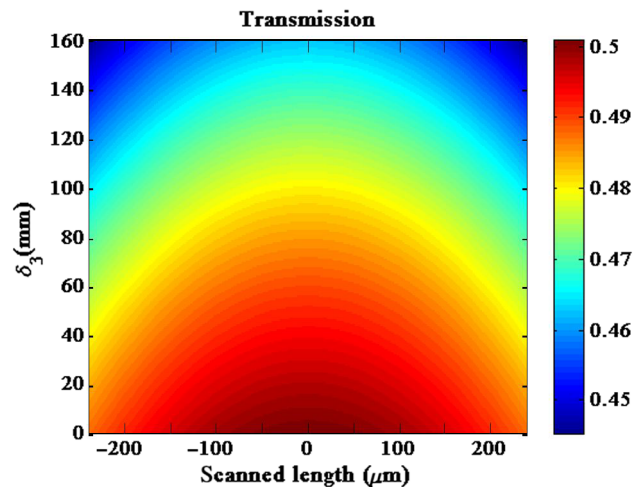$$M_R = \begin{pmatrix} d & b \\ c & a \end{pmatrix}.$$

(26)

Fig. 3 Transmission in function of δ_3 and the scanning distance for a fixed value of $\delta_2 = z_0/2$ ($z_0 = 35~\mu m$ = confocal parameter at the output of the fiber).

As d does not depend on δ_4, the selected value for δ_1 does not change from the computed before. Repeating the procedure for the complete round trip the coefficients A, B, C, D, E, and F, and the transmission was computed. The transmission as a function of the scanning distance and δ_4 were computed for a fixed value of $\delta_3 = 5$ mm and two values for δ_2 (0 and $z_0/2$). The transmission change with defocusing is similar to the one reported for the two-lens system, and the maximum transmission shift with δ_4, for different values of δ_2, is expected from the findings of similar correlations in the simplified two-lens system.[30] This fact can be clearly shown in Fig. 4 where the peak transmission is plotted versus the defocusing parameters, δ_2 and δ_4.

Finally, we included the sensitivity of the transmission to the parameter δ_5, which is the error in positioning the scan lens L_1 with respect to the camera plane of the microscope. The matrix M is

$$M = \begin{pmatrix} a & b \\ c & d \end{pmatrix}$$
$$= \begin{pmatrix} 1 & \delta_4 \\ 0 & 1 \end{pmatrix} \begin{pmatrix} \delta_5 \frac{f_{ob}}{f_{L2}f_{L1}} & -f_{ob}\frac{f_{L1}}{f_{L2}} + \delta_5 \frac{\delta_1 f_{ob}}{f_{L2}f_{L1}} \\ \frac{f_{L2}}{f_{ob}f_{L1}} - \delta_5 \frac{\Delta}{f_{L2}f_{ob}f_{L1}} & \frac{L_e}{2}\frac{f_{L2}}{f_{ob}f_{L1}} - \delta_5 \frac{\delta_1 \Delta}{f_{L2}f_{ob}f_{L1}} \end{pmatrix}$$
(27)

and again M_R is obtained by exchanging a with d.

Using this expression to compute the transmission as a function of the scanning length and δ_5 for $\delta_2 = \delta_4 = 0$ and $\delta_3 = 5$ mm (an easily achievable positioning accuracy), a maximum relative loss of 5% was found, for $|\delta_5| < 5$ mm, a condition easily achieved with the alignment procedure discussed below.

6 Alignment Procedure

In this section, the initial alignment procedure will be described based on previously exposed calculations. Once the system is assembled, the only parameters to be adjusted are the sample tilt and focus. The objectives of this protocol to be described are as follows: (1) to have the sample in focus in the entire field of view, (2) to have the probe beam focused at the center of the field of view when the beam goes through the central axis of the scanning system, (3) to keep the transmission as constant and as high as possible during the scanning of the beam. The components of the microscope and scanning units are shown in Fig. 2. The alignment requires seven steps as shown in the flowchart of Fig. 5.
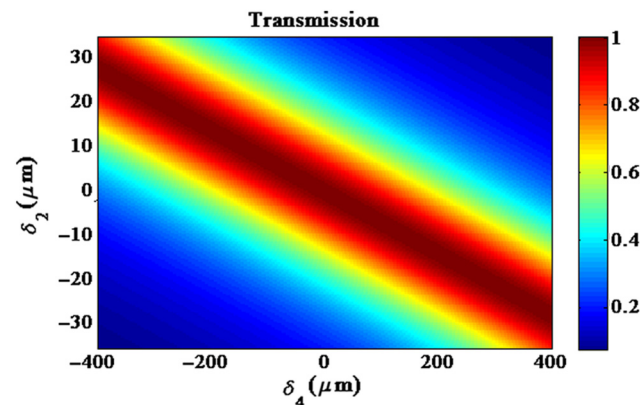

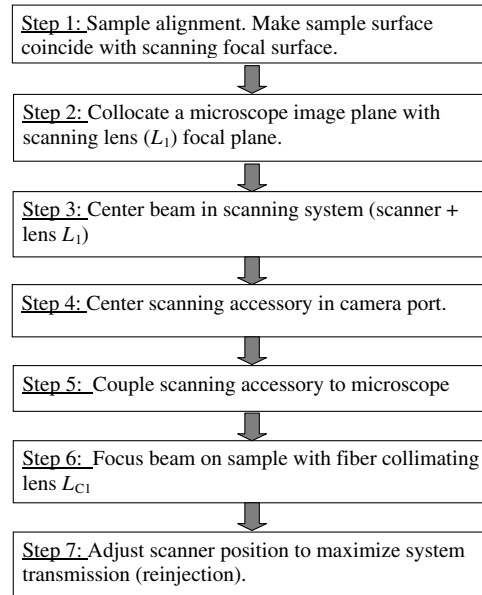**Fig. 4** Transmission in function of δ_2 and δ_4. ($\varepsilon = 0$).

Fig. 5 Flowchart illustrating the alignment procedure.

Step 1: Sample alignment. For inverted microscopes, this step is not necessary because the observation surface of the sample is set on the previously aligned surface of the microscope stage. Upright microscope was selected for our system because it allows the use of heating and cooling stages that are particularly useful for material science.

For the initial installation, a uniform flat-high-reflectivity sample is used, but it must have enough defects to allow the focusing with the camera. A mirror with pits is adequate. For this purpose, the sample stage must have a tilting platform. Alignment protocol:

a. Move the sample toward one side and focus it at the camera.

b. Translate the sample to the opposite side and refocus while measuring the total vertical displacement.

c. Return the focus to half the measured displacement.

d. The procedure is repeated until no further correction is needed.

The same protocol is used for the other tilting direction.

Step 2: The purpose is to locate the scanning lens L_1 so that its focal plane coincides with the camera plane of the microscope generated by the objective Ob and the tube lens L_2 (this corresponds to setting $\delta_5 = 0$). For this step, part of the scanning unit is disassembled and only the sections indicated as L_2, M_1, and L_1 are kept. The sample is illuminated with the microscope lamp and an image of the sample is projected through L_1 toward a screen located as far away as possible. The distance dx_P between the lens L_1 and the screen is measured. The proper position for L_1 is such that the image is located at infinity. Just using the thin lens equation, the correction needed for the desired condition can be computed as

$$\Delta(dx_P) = \frac{f_{L1}^2}{(dx_P - f_{L1})}. \tag{28}$$

Step 3: Alignment of the beams emerging from the fiber centered in the scanning unit optics. Use a centering pinhole mechanically designed to be placed at the center of the system at different locations.

    a. Center the beam with the angular stage A_1 at the first scanning mirror.

    b. Moving the scanning mirrors, center the beam at the pinhole located at the exit of the scanner, with the second scanning mirror center the beam at the pinhole located close to mirror M_1.

        These two steps are repeated until satisfactory alignment is met.

Step 4: Join the scanning unit to the microscope tube lens holder (in our system, it was detachable) and center the beam in the tube lens L_2. This is done using the angular alignment of unit A_2 that adjusts mirror M_1. For this step, detach the tube lens accessory from the microscope and check at a screen located several meters away that the beam hits the same point with and without the lens L_2.

Step 5: Couple the SA to the microscope. This must be done in such a manner that the centered beam hits the center of the visual field of the camera. This correction is made with the angular unit A_3, so that the prior alignment is not modified.

Step 6: A translation mechanism should be used with sensitivity at least 10 times better than the fiber confocal parameter z_0, which for our fiber was $z_0 = 35$ μm. Focus the probe beam with the sample focused at the camera. The small transmission of the dichroic mirror, DM, (designed to reflect the beams and transmit shorter wavelength for sample imaging) should be enough for this purpose.

Step 7: Adjust scanner position to maximize system transmission (reinjection). This is done by measuring in an oscilloscope the reinjected signal while the scanning mirrors are displaced. In Fig. 6, the amplitude
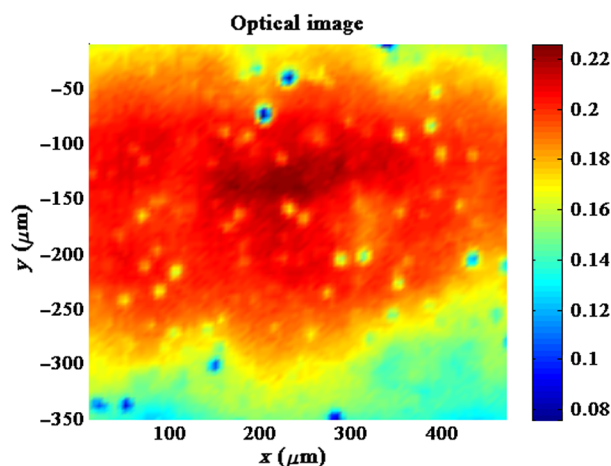
of the reinjected signal for a Pt-coated glass sample is shown when for one of the scanning mirrors $\delta_1 = \delta_{1i}$ and the second mirror results 10 mm ($2L_e$) away from such optimal position. The scan along the x-direction results almost with constant amplitude while the y scan shows a decrease in the reinjection with scanning angle. The target is to distribute the 10 mm between the two scanning mirrors. The fastest way is to program a diagonal scan of the mirrors with a range equal to the field of view of the camera. When one of the scanning mirrors is located at the best position, in the other mirror scanning direction, a loss will appear with the scan angle. Moving the unit to $\delta_1 = \delta_{1i}$ for the other mirror, which should be the construction distance between mirrors of the scanning unit, this position is recorded. Finally, the scanning unit is located at the middle point between the two positions determined before, and this will equally balance the losses in both directions.

7 Experimental

The following results are presented to show the performance of the system: a homogeneous glass sample to show the precision of the measurements, a sintered ceramic sample to show the different data that can be collected scanning a region as large as the camera field of view, and an amorphous metal foil ($Fe_{78}B_{13}Si_9$) that was scanned in temperature showing a phase transformation (glass to crystal).

To be able to collect information from the transparent glass sample, a 20-nm nominal thickness platinum film was deposited. This film acts as an absorbing layer but must be thin enough that no significant heat flow is propagated laterally within the film.[35] It was shown[30] that for near-infrared radiation the change in reflectivity with temperature can be neglected and the only contribution to the signal is due to the thermal expansion, as assumed in the model. A similar study was carried out with the visible wavelengths used in this setup and the same behavior was verified.[7,31] Hence, the thermal diffusivity can be retrieved by measuring the phase delay at a single frequency.

A histogram of the phase delay for the entire scanned area is shown in Fig. 7. The average phase delay resulted in -53.4 deg with a standard deviation of 1.19 deg. This uncertainty can be assigned to the instrument precision. The thermal diffusivity can be retrieved from the measurement of the phase delay, beam size, and modulation frequency with a sensitivity of 6%/deg.[7,31] In addition to the limitation in the precision arising from phase delay error, when converting to thermal diffusivity, the final accuracy is also limited by the error in the beam area measurement that in our case is 5%.

In Fig. 8, a set of four images obtained from a scan is shown for $UO_2 + 7.5\%Dy_2O_3$ sample using a $10\times$ objective, with a scanning speed of 1 s/pixel and a modulation frequency of 9737 Hz. The camera image is shown in Fig. 8(a), and the software developed allows scanning the same area showing the reinjected signal [Fig. 8(b)], the amplitude of the modulated signal [Fig. 8(c)] and the phase delay as filtered by the lock in amplifier [Fig. 8(d)]. The pixel size (step size for the scan) is 8.9 μm and the laser pump beam size is 8.8 μm. These data can be used

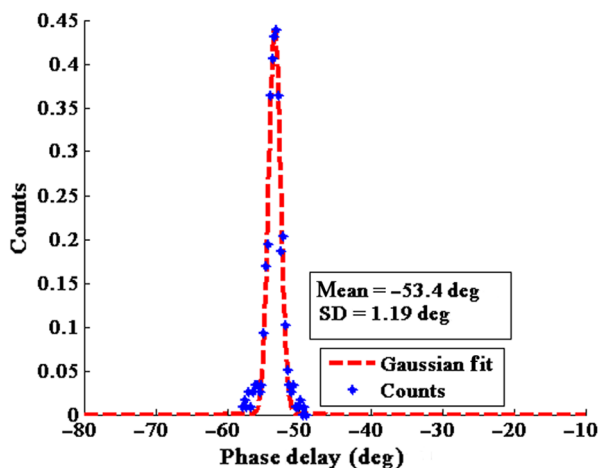**Fig. 6** Amplitude of the reinjected signal for a Pt-coated glass sample for $\delta_1 = \delta_{1i}$ for the x scanning mirror and $\delta_1 = \delta_{1i} + 2L_e$ for the y scanning mirror.

Fig. 7 Phase delay histogram for a 80-μm $\times$ 80-μm 80-μm scan on a uniform glass sample, coated with a 20-nm Pt film.

Fig. 9 Crystallization of an amorphous FeBSi sample. (a) Amplitude and (b) phase delay as function of temperature for a 15-K/min ramp. The crystallization peak is clearly seen at 840 $\pm$ 2 K.

to determine the thermal diffusivity map, homogeneity of the sintered sample, establish the presence of clusters, and identify the phases of such clusters.[6,7,31]

A final example is shown in Fig. 9, where signal amplitude and phase delay (at a fixed ω) are plotted as a function of temperature. A foil of a glassy metal alloy was placed in a heating microscope stage (Linkam TS 1500) and the temperature was ramped at a speed of 15 K/min. The signal change at a temperature of 840 $\pm$ 2 K can be assigned to the sample crystallization. In this case, the sample was not scanned, and the beam was kept focused at a single preselected spot. As the heating stage crucible expands with the temperature
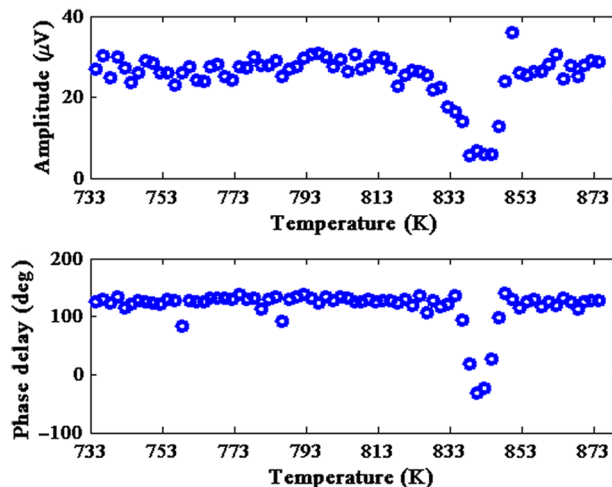
increase, the beam has to be kept in focus by means of a focus error measuring accessory based on a "blu ray" reading head inserted by a dichroic mirror between the lens LC1 and the scanner. The dichroic mirror reflected the violet (405 nm) beam from the "blu ray" head and transmitted the pump and probe beams. This was possible due to the flexibility in the parameter δ_3 determined before. To keep the sample in focus, the microscope fine focus screw was motorized and the software was adapted to correct using the error signal from the focus error device.
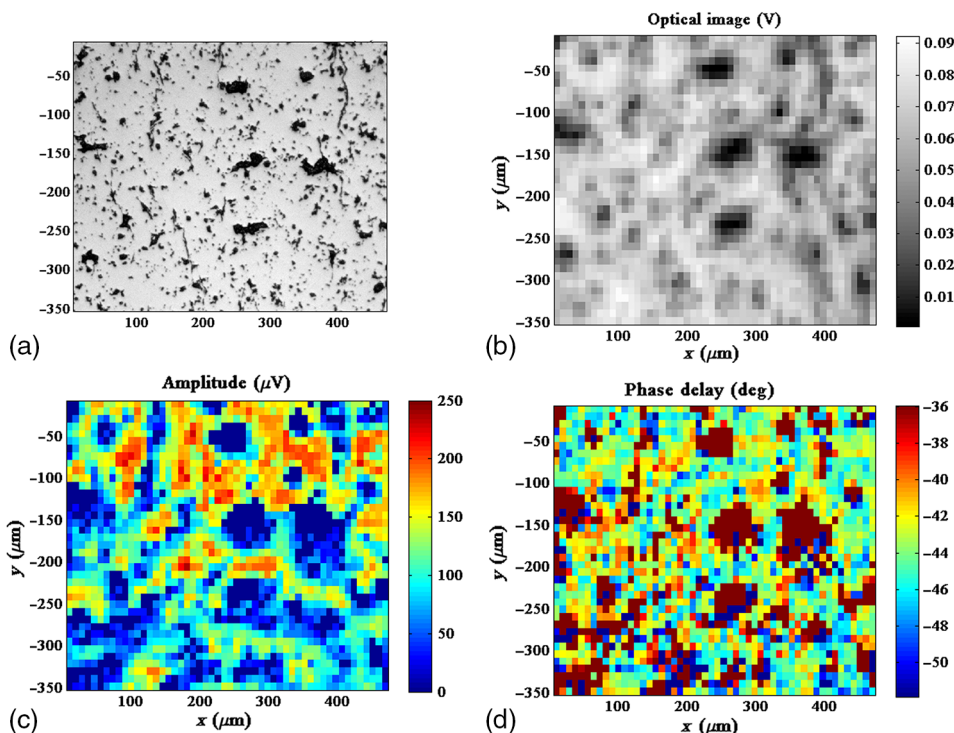

Fig. 8 Sample: UO$_2$ + 7.5%Dy$_2$O$_3$. (a) Camera image of the scanned region, (b) reinjected power map (reflectivity map), (c) signal: amplitude, (d) signal: phase delay. Pores yield no signal and those spots were assigned with a null value in the maps. A 10× objective was used and a step size of 8.9 μm.

8 Conclusions

An accessory for a commercial microscope has been presented that measures the thermal diffusivity and can be attached to a standard camera port. The technique is based on the determination of the curvature induced by the localized thermal expansion after heating the surface with a focused modulated laser. By using optical fiber components and fiber-coupled lasers, a robust optical device for beam delivery has been designed, which requires no internal alignment and provides construction collinear pump and probe beams. The same optical arrangement is used to collect the reflected probe beam, and fiber-optic devices separate the returning probe beam toward the detector. A scanning mirror assembly similar to the systems used in standard scanning confocal microscopes was added. The confocal collection with fiber optics has specific requirements that are more restrictive than pinhole collection, and the detailed design equations have been discussed, providing information on which the sensitive parameters regarding the positioning and alignment of the optical elements that couple the beams to the microscope. It was shown that due to the location of the tube lens in commercial microscopes, the construction distance between scanning mirrors and the defocusing required by the technique, the scanning lens has to be located at particular positions and the fiber collimating lens has a limited range where it can be placed. Otherwise, the reinjected probe power changes significantly with the scan, reducing the practical scanning area of the sample. With the design described, a scan area as large as the field of view of the microscope camera was achieved.

The initial alignment procedure was discussed in detail. The system results are so robust that no further alignment is necessary for the day-to-day use, becoming a tool that can be used for routine quality control, operated by a trained technician.

The precision of the system in determining the phase delay (that is used to retrieve the thermal diffusivity) was measured to be 1 deg, which corresponds to a 5% error in the thermal diffusivity. Mapping a sintered mixed oxide sample, the capabilities of the system were demonstrated. The analysis of the allowed positioning range for the collimating lens yielded a tolerance of up to 150 mm, which permitted the introduction of a focus correction device, which was mandatory for the addition of a heating stage since permanent focus control is necessary due to the thermal expansion of the system. This device was used to determine phase-transition temperature of a test sample.

References

1. Y. Liu et al., "Remote quantitative temperature and thickness measurements of plasma-deposited titanium nitride thin coatings on steel using a laser interferometric thermoreflectance optical thermometer," *Rev. Sci. Instrum.* **76**, 084902 (2005).
2. N. Taketoshi, T. Baba, and A. Ono, "Development of a thermal diffusivity measurement system for metal thin films using a picosecond thermoreflectance technique," *Meas. Sci. Technol.* **12**, 2064–2073 (2001).
3. P. Martinez, A. Mandelis, and J. J. Alvarado-Gil, "Optical and thermal depth profile reconstructions of inhomogeneous polymerization in dental resins using photothermal waves," *J. Appl. Phys.* **108**, 054902 (2010).
4. R. Cellorio et al., "Accurate reconstruction of the thermal conductivity depth profile in case hardened steel," *J. Appl. Phys.* **107**, 083519 (2010).
5. C. Glorieux et al., "Depth profiling of thermally inhomogeneous materials by neural network recognition of photothermal time domain data," *J. Appl. Phys.* **85**, 7059–7063 (1999).
6. F. Z. Escola et al., "Photothermal microscopy applied to the characterization of nuclear fuel pellets," *J. Nucl. Mater.* **435**, 17–24 (2013).
7. F. Z. Escola et al., "Photothermal microscopy," *Procedia Mater. Sci.* **8**, 665–673 (2015).
8. C. Wei et al., "Micron resolution spatially resolved measurement of heat capacity using dual-frequency time-domain thermoreflectance," *Rev. Sci. Instrum.* **84**, 071301 (2013).
9. S. Huxtable et al., "Thermal conductivity imaging at micrometre-scale resolution for combinatorial studies of materials," *Nat. Mater.* **3**, 298–301 (2004).
10. U. Crossa Archiopoli, N. Mingolo, and O. E. Martínez, "Two-dimensional imaging of thermal diffusivity in metals by scanning photodeflection detection," *J. Appl. Phys.* **107**, 023520 (2010).
11. U. Crossa Archiopoli, N. Mingolo, and O. E. Martínez, "Two-dimensional mapping of micro-hardness increase on surface treated steel determined by photothermal deflection microscopy," *Surf. Coat. Technol.* **205**, 3087–3092 (2011).
12. C. Wang and A. Mandelis, "Characterization of hardened cylindrical C1018 steel rods (0.14-0.2% C, 0.6-0.9% Mn) using photothermal radiometry," *Rev. Sci. Instrum.* **78**, 054902 (2007).
13. J. C. Krapez and R. Li Voti, "Effusivity depth profiling from pulsed radiometry data: comparison of different reconstruction algorithms," *Anal. Sci.* **17**(Special Issue), S417–S418 (2001).
14. D. Boyer et al., "Photothermal imaging of nanometer-sized metal particles among scatterers," *Science* **297**, 1160–1163 (2002).
15. A. Gaiduk et al., "Detection limits in photothermal microscopy," *Chem. Sci.* **1**, 343–350 (2010).
16. C. Pache et al., "Fast three-dimensional imaging of gold nanoparticles in living cells with photothermal optical lock-in optical coherence microscopy," *Opt. Express* **20**, 21385 (2012).
17. L. Cognet et al., "Single metallic nanoparticle imaging for protein detection in cells," *Proc. Natl. Acad. Sci. U. S. A.* **100**, 11350–11355 (2003).
18. J. M. Tucker-Schwartz et al., "In vivo photothermal optical coherence tomography of gold nanorod contrast agents," *Biomed. Opt. Express* **3**, 2881–2895 (2012).
19. J. Yang, C. Maragliano, and A. J. Schmidt, "Thermal property microscopy with frequency domain thermoreflectance," *Rev. Sci. Instrum.* **84**, 104904 (2013).
20. A. J. Schmidt, R. Cheaito, and M. Chiesa, "A frequency-domain thermoreflectance method for the characterization of thermal properties," *Rev. Sci. Instrum.* **80**, 094901 (2009).
21. A. Rosencwaig et al., "Detection of thermal waves through optical reflectance," *Appl. Phys. Lett.* **46**, 1013–1015 (1985).
22. J.-C. Zhao, X. Zheng, and D. G. Cahill, "Thermal conductivity mapping of the Ni-Al system and the beta-NiAl phase in the Ni-Al–Cr system," *Scr. Mater.* **66**, 935–938 (2012).
23. X. Zheng et al., "High-throughput thermal conductivity measurements of nickel solid solutions and the applicability of the Wiedemann-Franz law," *Acta Mater.* **55**, 5177–5185 (2007).
24. A. Salazar, A. Sánchez-Lavega, and J. Fernández, "Thermal diffusivity measurements in solids by the 'mirage' technique: experimental results," *J. Appl. Phys.* **69**, 1216–1223 (1991).
25. X. Zheng et al., "Micron-scale measurements of the coefficient of thermal expansion by time-domain probe beam deflection," *J. Appl. Phys.* **104**, 073509 (2008).
26. A. Rosencwaig, J. Opsal, and D. L. Willenborg, "Thin-film thickness measurements with thermal waves," *Appl. Phys. Lett.* **43**, 166–168 (1983).
27. J. Opsal, A. Rosencwaig, and D. L. Willenborg, "Thermal-wave detection and thin-film thickness measurements with laser beam deflection," *Appl. Opt.* **22**, 3169–3176 (1983)
28. O. E. Martínez, F. Balzarotti, and N. Mingolo, "Thermoreflectance and photodeflection combined for microscopic characterization of metallic surfaces," *Appl. Phys. B* **90**, 69–77 (2008).
29. N. Mingolo and O. E. Martínez, "Focus shift photothermal method for thermal diffusivity mapping," *J. Appl. Phys.* **111**, 123526 (2012).
30. N. Mingolo and O. E. Martínez, "Thermal expansion recovery microscopy: practical design considerations," *Rev. Sci. Instrum.* **85**, 014903 (2014).
31. F. Z. Escola et al., "Characterization of sintered mixed oxides by photothermal microscopy" *Int. J. Thermophys.* **37**, 20 (2016).
32. W. B. Amos, "Achromatic scanning system," US Patent 4997242 A (1990).
33. A. E. Siegman, *Lasers*, University Science, Mill Valley, California (1986).
34. A. B. Buckman, *Guided-Wave Photonics*, p. 150, Saunders, Philadelphia, Pennsylvania (1992).
35. E. A. Domené et al., "Photothermal measurement of absorption and scattering losses in thin films excited by surface plasmons," *Opt. Lett.* **34**, 3797–3799 (2009).

Facundo Zaldívar Escola received his degree of Licenciado en Física (MS) and PhD in engineering from the University of Buenos Aires, Buenos Aires, Argentina, in 2011, and 2016, respectively. He has worked in the development of photothermal methods for materials characterization.

Darío Kunik received his degree of Licenciado en Física (MS) and PhD in physics from the University of Buenos Aires, Buenos Aires, Argentina, in 2004, and 2009, respectively. After a postdoctoral position at the University of Montreal from 2009 to 2011, he joined the CONICET in 2012 as a research fellow at Tolket SRL. Currently, he is in charge of the Photonics Sensors Labs, YPF Tecnología. His areas of interest include optical sensors and microscopy.

Nelly Mingolo received his degree of Licenciado en Física (MS) and PhD in physics from the University of Buenos Aires, Buenos Aires, Argentina, in 1981, and 1992, respectively. She has worked on amorphous metals and fast-quenching techniques, as well as characterization techniques. Currently, she is a professor at the University of Buenos Aires and head of the Directed Beam Laboratory.

Oscar Eduardo Martínez received the Computador Científico, the degree of Licenciado en Física (MS), and PhD in physics from University of Buenos Aires, Buenos Aires, Argentina, in 1975, 1976, and 1982, respectively. Currently, he is a professor at the University of Buenos Aires and a member of the research staff of Consejo Nacional de Investigaciones Científicas y Tecnológicas de la República Argentina. He has published more than 100 papers, mainly on ultrashort pulse generation and nanophotonics.